# Motion Correction in Dual Gated Cardiac PET using Mass-Preserving Image Registration

Fabian Gigengack*, Lars Ruthotto†, Martin Burger‡, Carsten H. Wolters§, Xiaoyi Jiang¶ and Klaus P. Schäfers‖

November 9, 2011

**Abstract**

Respiratory and cardiac motion leads to image degradation in positron emission tomography (PET) studies of the human heart. In this paper we present a novel approach to motion correction based on dual gating and mass-preserving hyperelastic image registration. Thereby, we account for intensity modulations caused by the highly non-rigid cardiac motion. This leads to accurate and realistic motion estimates which are quantitatively validated on software phantom data and carried over to clinically relevant data using a hardware phantom. For patient data, the proposed method is first evaluated in a high statistic (20 minutes scans) dual gating study of 21 patients. It is shown that the proposed approach properly corrects PET images for dual - cardiac as well as respiratory - motion. In a second study the list mode data of the same patients is cropped to a scan time reasonable for clinical practice (3 minutes). This low statistic study not only shows the clinical applicability of our method but also demonstrates its robustness against noise obtained by hyperelastic regularization.

Keywords: motion correction, mass-preservation, dual gating, image registration, hyperelastic regularization, PET

*F. Gigengack (fabian.gigengack@uni-muenster.de) is with the European Institute for Molecular Imaging (EIMI) and the Dept. of Mathematics and Computer Science, University of Münster, Germany. This work was partly funded by the Deutsche Forschungsgemeinschaft, SFB 656 MoBil (projects B2 and B3) and projects BU2327/2-1, JU445/5-1 and WO1425/1-1. *Asterisk indicates corresponding author.*

†L. Ruthotto is with the Institute of Mathematics and Image Computing (MIC), University of Lübeck, Germany

‡M. Burger is with the Institute for Computational and Applied Mathematics, University of Münster, Germany

§C.H. Wolters is with the Institute for Biomagnetism and Biosignalanalysis, University of Münster, Germany

¶X. Jiang is with the Dept. of Mathematics and Computer Science, University of Münster, Germany

‖K. P. Schäfers is with the European Institute for Molecular Imaging (EIMI), University of Münster, Germany

# 1 Introduction

Positron emission tomography (PET) requires relatively long image acquisition times in the range of minutes. Hence, motion affects the spatial localization of the emission events and degrades the images. In thoracic PET both respiratory and cardiac motion lead to spatially blurred images. In the literature, maximal displacements of 23 mm (average $15 - 20$ mm) for respiratory [53], and even 42 mm (average $8 - 23$ mm) for cardiac motion [61] are reported. The consideration of motion becomes more and more important, given the ever improving spatial resolutions in modern scanning systems (currently about $4 - 5$ mm full width at half maximum (FWHM)).

In contrast to PET images, CT images hardly suffer from motion as they are usually acquired during breath holding and can be corrected for cardiac motion by prospective electrocardiogram (ECG) triggering. In the presence of severe motion, computed tomography (CT) based attenuation correction can thus lead to considerable image artifacts [15, 7, 47, 48, 23].

To reduce motion artifacts in PET, gating based techniques were found applicable [38]. Gating is the decomposition of the whole dataset into parts that represent different breathing and/or cardiac phases [11]. After gating each single gate shows less motion, however, suffers from a relatively low signal to noise ratio (SNR) as only a small portion of all available events is contained. The fact that images contain both cardiac and respiratory motion motivates the reduction of both types by means of dual gating [43].

The impact of motion and gating on image quality is illustrated in Fig. 1. A coronal slice of the human heart (20 minutes $^{18}$F-FDG PET scan without attenuation correction) is shown. In (a), a reconstruction of the whole dataset without gating can be seen. Respiratory and cardiac motion causes an obvious blurring of the heart contour. In contrast, a single phase out of the respiratory and cardiac cycle (dual gating with five respiratory and five cardiac gates) is shown in (b). The blurring is considerably reduced. This phenomenon is further illustrated with line profiles in (d). The maximum peaks of the dash-dotted profile (no gating) are clearly lower compared to the dashed profile (single gate). Furthermore, motion leads to an apparently higher blood pool activity in the image without gating compared to the gated and motion corrected image. A preview of the result after applying our method (VAMPIRE) is given in (c).

## 1.1 Related Work: Motion Correction in Cardiac PET

To reduce motion in cardiac PET and its effects on further analysis, several approaches were proposed recently. Almost all approaches have in common that motion is estimated on basis of the PET data instead of, e.g., gated CT images, in order to keep the radiation burden as low as possible. They can be classified into four groups [6]:

1. Averaging of aligned images

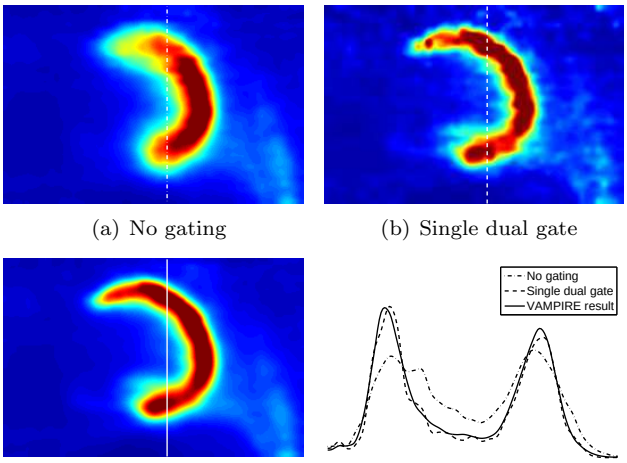


(a) No gating (b) Single dual gate

(c) Our result (VAMPIRE) (d) Line profiles

Figure 1: Coronal slices of reconstructions from (a) whole data, (b) one single respiratory and cardiac phase, and (c) after applying our motion correction method that combines the advantages of both images in (a) and (b): reduced motion and a low noise level. This is further illustrated with line profiles (d).

2. Re-reconstruction using a time-varying system matrix

3. Event rebinning

4. Joint reconstruction of image and motion

1) After gating the data, each gate is reconstructed individually and aligned to one assigned reference gate. To overcome the problem of low SNRs, the aligned images are averaged (summed) afterwards. In the context of respiratory motion correction, Dawood et al. [15] propose an optical flow based approach and Bai et al. [6, 4, 5] use a regularized B-spline approach with a Markov random field regularizer. In the context of cardiac motion correction, Klein et al. [31, 29] propose a technique using 3D optical flow and by modeling the myocardium as an elastic membrane. In their approach intensity modulations caused by cardiac motion (see 1.2) are not addressed.

2) Similar to 1), gating is applied and each individually reconstructed gate is aligned to one assigned reference gate. The obtained motion information is incorporated into a subsequent re-reconstruction of the whole dataset. The lines of response are adjusted according to the motion field which implies time-varying system matrices, see [36, 20] for respiratory motion correction approaches.

3) The acquired list mode data is gated and each gate is reconstructed. Motion is estimated based on these reconstructed images. The initial list mode data is rebinned in a subsequent step by applying the transformation gained from the motion estimation step [35]. As only affine transformations are allowed,

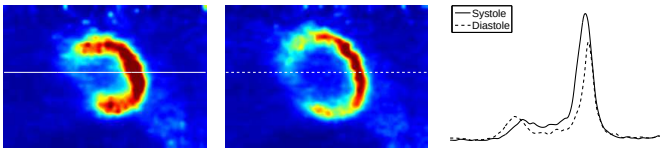


(a) Systole (b) Diastole (c) Line profiles

Figure 2: Coronal slices of the systole (a) and diastole (b) and corresponding line profiles (c) are shown for one patient. The solid line belongs to the systole and the dashed line to the diastole. It can be observed that the maximum peaks in these line profiles vary a lot due to the PVE.

such methods can correct for respiratory motion (which is primarily locally rigid) to a certain extent but not for non-linear cardiac motion.

4) In joint reconstruction, motion is estimated simultaneously to the reconstruction of the image [8, 10, 52, 26, 41]. An objective function is optimized in two arguments: image and motion. Hence, only *one* image with the full statistic is reconstructed. A drawback of these approaches are the relatively high computational costs.

## 1.2 Mass-Preservation

Tissue compression and the partial volume effect (PVE) lead to intensity modulations [42]. Especially for relatively small structures like the myocardium the true uptake values are affected by the PVE. An example is given in Fig. 2 where a systolic and diastolic slice (same respiratory phase) of a dual gated 3D dataset and line profiles are shown. Especially the maximum intensity values of the two heart phases indicate that corresponding points can differ in intensity.

To overcome the intensity artifacts, the mass-preserving property of PET images has to be identified. In gating, all gates (for any gating approach) are formed over the same time interval. Hence, the total amount of radioactivity in each phase is approximately equal. In other words, in any respiratory and/or cardiac gate no radioactivity can be lost or added apart from some minor changes at the edges of the field of view, which is referred to as *mass-preservation* in the following.

## 1.3 Related Work: Mass-Preservation

The approaches discussed in 1.1 do not discuss the intensity modulation problem explicitly. Apart from [31, 29, 41], even all of the above methods treat only respiratory motion. However, mass-preserving transformation models were already applied to different kinds of medical data, including CT, single photon emission computed tomography (SPECT), and magnetic resonance imaging (MRI).

CT: A mass-preserving registration framework for CT lung images with an additional mapping of the Hounsfield units to density values was presented in [62]. Yin et al. applied successfully a mass-preserving multilevel B-spline approach in a multiresolution formulation. Apart from a displacement constraint which ensures bijectivity, they do not mention any regularization of the B-spline transformation like, e.g., in [6].

SPECT: An expansion ratio was incorporated into the objective function in [42, 59]. The expansion ratio is the ratio of volumetric change and guarantees the preservation of radioactivity respectively mass.

MRI: Recently, mass-preserving transformations were successfully applied to reduce image degradation in MRI due to field inhomogeneities [50, 46, 12]. In these works, mislocalizations are restricted along one line and have reversed effects in two reference scans.

For PET, we developed the Variational Algorithm for Mass-Preserving Image REgistration (VAMPIRE) which was firstly described by us in [50, 22]. As cardiac motion is one component of dual motion, the present paper can be understood as an extension of the cardiac motion correction proposed in [22]. Apart from the changed data basis (cardiac vs. dual gating; enlarged patient number), the extension consists of an extensive validation (software and hardware phantom) and the incorporation of hyperelastic regularization. The hyperelasticity features diffeomorphic transformations which becomes especially important for images with low statistics as occurring in dual gating scenarios with their high number of gates. The idea of VAMPIRE (i.e., mass-preserving image registration) is, in addition to deforming the template volume, the multiplication by the transformation's Jacobian determinant $\det(\nabla y)$. Motivated by the integration by substitution theorem for multiple variables, the Jacobian determinant expresses the volumetric change due to the transformation $y$. In the following we refer to $\det(\nabla y)$ as the Jacobian map. The comparison with other methods is not discussed in the following, since this was already done for standard image registration in [22].

Thielemans et al. [58] also proposed to incorporate the Jacobian determinant into the registration functional, but with a significantly different numerical realization, i.e., the determinant is approximated by $\det(\nabla y) \approx 1 + \mathrm{tr}(\nabla d)$, where $y(x) = x + d(x)$. For small deformations the approximation is certainly sufficient. Due to the relatively large local deformations in cardiac PET as discussed before, one can be faced with large deformation vectors. During the development of our methods we also implemented the approximation and observed problems with large motion especially during optimization. Therefore, it is preferable to choose the exact calculation. In our approach, the full Jacobian determinant is discretized.

The background of applying mass-preservation transformation models in PET imaging varies slightly from the approaches for CT and MRI. In CT, the algorithms compensate for tissue compression only and in MRI for field inhomogeneities. In PET and SPECT, mass-preservation also compensates for tissue compression, but in addition allows the matching of corresponding points with PVE disturbed intensities. It should be noted that we do not correct for the

PVE with our method. Approaches that correct for the PVE could be applied in advance to potentially improve the motion estimation. The partial volume correction can be applied during reconstruction [1] (resolution recovery) or post-reconstruction [9] (filtering). However, in these approaches thin structures still suffer from tissue fraction due to the limited resolution and further, the recovery of resolution typically results in an elevated amount of noise.

Recently, Dawood et al. [39] extended their optical flow method [15] by a mass-preserving constraint using a continuity equation. Their results achieved for cardiac motion correction are well in line with our previous work [22] and further motivate the extension of our method to dual gated PET in this paper to diminish motion to a higher extent. Technically, optical flow and image registration approaches provide significantly different approaches to motion estimation. We choose the image registration framework as it simplifies the incorporation of physically meaningful regularization like hyperelasticity.

For completeness, the work of Klein [27, 28] should be mentioned. A forward deformation mapping is utilized which assures the preservation of mass. As such a transformation model is not necessarily surjective, a sampling of each point in the reference domain is not guaranteed. Furthermore, a complicated energy function with numerous local minima due to the forward deformation mapping is reported.

## 1.4 Related Work: Diffeomorphic Registration

In medical image registration, diffeomorphic transformations are imperative as they are smooth, invertible, orientation preserving, free of foldings, etc. Recently, several approaches were developed to ensure diffeomorphisms [2, 3, 45, 49]. Inspired by the Jacobian determinant in VAMPIRE, we derived a new discretization of a hyperelastic regularizer [18] that is now integrated in FAIR. It directly controls the volumetric change which in our case corresponds to the intensity modulations. Although it is a key feature of VAMPIRE, it can also be used for any other registration task. The main ideas of this regularizer are summarized in Sec. 2.2.

## 1.5 Our Method

In this paper we present an image registration based motion correction approach for dual gated PET. Hence, respiratory *and* cardiac motion are reduced significantly by the following strategy:

1. Dual gating
2. Mass-preserving motion estimation (VAMPIRE)
3. Averaging of the aligned images

The key contribution is the novel image registration approach VAMPIRE that is used for accurate motion estimation. VAMPIRE incorporates the identified

mass-preserving property of PET into a variational formulation of the image registration problem. Due to the mass-preservation, VAMPIRE depends - even more than standard registration approaches - on the invertibility of the transformation, which is required to model the physiological motion of body tissue. In our application we further deal with noisy data with large and nonlinear inherent deformations. These requirements complicate proper regularization and motivate the restriction to diffeomorphic registration schemes. The hyperelastic regularizer in FAIR was used for VAMPIRE.

The accuracy and efficiency of the derived method is validated on phantom data and is applied to real patient data in two group studies. It is shown that the proposed method enhances the images even for short acquisition times.

# 2 Materials and Methods

The idea behind mass-preserving registration is described first in this section. Subsequently, the phantom and human patient data and dual gating will be addressed. Methods for evaluation of our findings are discussed at the end of this section.

## 2.1 VAMPIRE - Variational Algorithm for Mass-Preserving Image REgistration

For motion correction, a template image $\mathcal{T} : \Omega \to \mathbb{R}$ is registered onto an assigned reference image $\mathcal{R} : \Omega \to \mathbb{R}$, where $\Omega \subset \mathbb{R}^d$ is the image domain and $d$ the dimension (in our case $d = 3$). This yields a transformation $y : \mathbb{R}^d \to \mathbb{R}^d$ representing point-to-point correspondences between $\mathcal{T}$ and $\mathcal{R}$. To find $y$, the following functional has to be minimized

$$\min_y \ \mathcal{D}(\mathcal{M}(\mathcal{T}, y),\ \mathcal{R}) + \alpha\, \mathcal{S}(y)\ . \tag{1}$$

Here $\mathcal{D}$ denotes the distance functional and $\mathcal{M}$ the transformation model. $\mathcal{S}$ is the regularization functional. $\mathcal{D}$ measures the dissimilarity between the transformed template image and the fixed reference image. Since both images, i.e., $\mathcal{T}$ and $\mathcal{R}$, are of the same modality in our case, we can use the sum-of-squared differences (SSD) as a distance functional $\mathcal{D}$.

**Definition 1 ($\mathcal{D}^{\mathbf{SSD}}$)** *The* sum of squared differences $\mathcal{D}^{SSD}$ *of two images* $\mathcal{T}$ *and* $\mathcal{R}$ *is defined as*

$$\mathcal{D}^{SSD}(\mathcal{T}, \mathcal{R}) := \frac{1}{2} \int_\Omega (\mathcal{T}(x) - \mathcal{R}(x))^2 dx\ . \tag{2}$$

Using the SSD measure in the distance functional entails the assumption of similar intensities at corresponding points. However, this assumption does not hold for dual gated PET as discussed in connection with Fig. 2. Thus, the standard image registration model $\mathcal{M}^{\text{std}}(\mathcal{T}, y) := \mathcal{T} \circ y = \mathcal{T}(y)$ needs some modification to express this feature.

VAMPIRE incorporates a mass-preserving component by accounting for the volumetric change induced by the transformation $y$. We know by the integration by substitution theorem for multiple variables

$$\int_{y(\Omega)} \mathcal{T}(x)dx = \int_{\Omega} \mathcal{T}(y(x)) \, |\det(\nabla y(x))| \, dx \, . \tag{3}$$

Referred to PET, (3) guarantees the same total amount of radioactivity before and after applying the transformation $y$ to $\mathcal{T}$. As $y$ should reflect cardiac and respiratory motion, transformations that are not one-to-one are anatomically not meaningful and have therefore to be excluded. In our approach, the hyperelastic regularization guarantees $y$ to be diffeomorphic and orientation preserving, which allows us to drop the absolute value bars

$$\int_{y(\Omega)} \mathcal{T}(x)dx = \int_{\Omega} \mathcal{T}(y(x)) \, \det(\nabla y(x)) \, dx \, . \tag{4}$$

In the mass-preserving transformation model of VAMPIRE the template image $\mathcal{T}$ is transformed by interpolation on the deformed grid $y$ with an additional multiplication by the volumetric change.

**Definition 2 ($\mathcal{M}^{\mathbf{MP}}$)** *For an image $\mathcal{T}$ and a transformation $y$ the* mass-preserving transformation model *is defined as*

$$\mathcal{M}^{MP}(\mathcal{T}, y) := (\mathcal{T} \circ y) \cdot \det(\nabla y) = \mathcal{T}(y) \cdot \det(\nabla y) \, . \tag{5}$$

The multiplication by the Jacobian is a physiological and realistic modeling for density based images [62, 58].

The calculation of the first and second derivatives are required for fast minimization of the functional in (1) during optimization. The first derivatives are calculated analytically and second derivatives are approximated as described in [44] such that the Hessian system is positive definite.

**Remark 1 (First variation)** *Let $\mathcal{T}, \mathcal{R} \in C^1(\Omega, \mathbb{R})$ be continuously differentiable images and the transformation $y \in C^2(\Omega, \mathbb{R}^3)$ be twice continuously differentiable. The first variation of the distance functional $\mathcal{D}^{SSD}(\mathcal{M}^{MP}(\mathcal{T}, y), \, \mathcal{R})$ is given by*

$$\frac{\partial \mathcal{D}^{SSD}}{\partial y} = r(y) \cdot \det(\nabla y) \cdot \nabla \mathcal{T} - \operatorname{div}(r(y) \cdot \mathcal{T} \cdot \nabla \det(\nabla y)) \, , \tag{6}$$

*where $r(y) := \mathcal{M}^{MP}(\mathcal{T}, y) - \mathcal{R}$ denotes the residual and $\operatorname{div}(\,\cdot\,)$ the divergence.*

## 2.2 Hyperelastic regularization

As an under-determined inverse problem, non-linear image registration demands for regularization [21]. Polyconvex hyperelastic regularization [14, 18] of the transformation $y$ is used to guarantee the well-posedness of (5), to improve the robustness against noise and to enforce realistic cardiac and respiratory motion. The regularization functional $\mathcal{S}^{\text{hyper}}$ controls changes in length, area of the surface and volume of $y$.

**Definition 3 ($\mathcal{S}^{\mathbf{hyper}}$)** *Let $\alpha_l, \alpha_a, \alpha_v > 0$ be constants and $p, q \geq 2$[1]. Further let $\Gamma_a, \Gamma_v : \mathbb{R} \to \mathbb{R}$ be positive and strictly convex functions, with $\Gamma_v$ satisfying $\lim_{z\to 0^+} \Gamma_v(z) = \lim_{z\to\infty} \Gamma_v(z) = \infty$ . The* hyperelastic *energy caused by the transformation $y : \mathbb{R}^d \to \mathbb{R}^d$ is defined as*

$$\begin{aligned}\mathcal{S}^{hyper}&(y, \alpha_l, \alpha_a, \alpha_v)\\ &= \alpha_l \cdot \mathcal{S}^{length}(y) + \alpha_a \cdot \mathcal{S}^{area}(y) + \alpha_v \cdot \mathcal{S}^{vol}(y).\end{aligned} \tag{7}$$

*The three summands individually control changes in length, area of the surface and volume,*

$$\mathcal{S}^{length}(y) := \int_\Omega \|\nabla y\|_2^p \, dx \tag{8}$$

$$\mathcal{S}^{area}(y) := \int_\Omega \Gamma_a(\|Cof(\nabla y)\|_2^q) \, dx \tag{9}$$

$$\mathcal{S}^{vol}(y) := \int_\Omega \Gamma_v(\det(\nabla y)) \, dx \, , \tag{10}$$

*where the Frobenius norm is defined as $\|A\|_2 := \sqrt{\mathrm{tr}(A^T A)}$ for matrices $A \in \mathbb{R}^{d\times d}$ and $Cof(A)$ denotes the cofactor matrix.*

For $\alpha_v > 0$, the conditions for $\Gamma_v$ claimed above ensure $\det(\nabla y) > 0$, i.e., $y$ is a diffeomorphism [18]. This allows us to omit the absolute value bars in (4). A method for determining the $\alpha$-parameters is described in Section 2.8.

In the formulation (1) the positive real number $\alpha$ balances between minimizing the SSD and retaining smooth and realistic transformations. As each term of the hyperelastic regularizer has an individual weighting factor we chose $\alpha = 1$ and determine only $\alpha_l$, $\alpha_a$, and $\alpha_v$ (see 2.8).

## 2.3 Implementation and Runtime

The VAMPIRE implementation is based on the freely available FAIR toolbox [44] in MATLAB®. In order to improve robustness against local minima and to speed up the optimization, a multi-level strategy (multiple image resolutions) is used along with a Gauss-Newton optimization. Further, a 3D spline-interpolation scheme with moments regularization is chosen to ensure differentiability and provide robustness against noise [44]. The regularization parameter $\theta$ of the spline interpolation was set to 0.5 throughout this paper. Some time critical operations, like interpolation and regularization, were implemented matrix free and parallelized in C to keep memory usage to a minimum and to speedup the computation.

All computations were evaluated on a quad-core 64-bit Linux machine with 2.50 GHz and 7.5 GB RAM. Some concrete values will be given in the results section.

[1] The parameters were set to $p = q = 2$ throughout this paper.

## 2.4 XCAT Phantom Data

We evaluate the VAMPIRE algorithm on two kinds of phantom data. The established XCAT software phantom [54, 55] and a PET hardware phantom (Section 2.5) were used to validate the applicability of VAMPIRE for motion correction in PET.

With the XCAT phantom, two gates with male anatomy were generated that vary in the respiratory as well as the cardiac phase. One template image $\mathcal{T}$, showing the systolic heart phase at maximum inspiration, and a reference image $\mathcal{R}$ in the diastolic heart phase at mid-expiration, see Fig. 3(a) and (c). Taking the mid-expiration phase as reference was suggested in [16] as it minimizes the average motion to the other respiratory phases.

The maximum diaphragm motion was set to 20 mm and the voxel size to 3.375 mm. The total size of the volumes is $175 \times 175 \times 47$.

The XCAT phantom data was trimmed to be comparable to the patient data introduced in Section 2.6 in terms of

1. Tracer distribution: The tracer distribution was estimated on basis of the patient data. For each organ (i.e. heart, lungs, liver), bones, and the background, a small region of interest (ROI) was evaluated to estimate the local tracer distribution.

2. Noise: The noise level in the patient data was estimated by measuring the SNR in a background ROI. The SNR of the phantom data (also measured in a background ROI) was adapted by controlling the amount of Poisson noise.

3. Scanning system: The same scanner was modeled and the same reconstruction software with the same parameters was used.

This allows a meaningful parameter selection for the patient data using the ground-truth information about the transformation provided by the XCAT phantom, cf. Section 2.8. To validate the parameter selection with the XCAT phantom, a second set of images was generated as described above, but with female anatomy. The female anatomy is used for analyzing the robustness of the parameter selection to natural anatomical variations.

The ideal images of the XCAT tool were blurred with a Gaussian kernel to simulate the PVE. To this end, we computed a full width at half maximum (FWHM) comparable to the FWHM of the scanner used for the patient data, see Section 2.6. According to [13], this results in a FWHM of

$$R_{sys} \approx \sqrt{R_{int}^2 + \Delta_{nc}^2 + \Delta_{pos}^2} \approx 3.85\,\text{mm}\,, \tag{11}$$

where the internal resolution is $R_{int} = 6.75\,\text{mm}/2$ (detector width of 6.75 mm), blurring due to photon noncolinearity is $\Delta_{nc} = 0.0022 \cdot 838\,\text{mm}$ (838 mm is the diameter of the scanner), and the blurring due to the positron range of $^{18}$F-FDG has a FWHM of $\Delta_{pos} = 0.102\,\text{mm}$. The blurred images were forward projected into measurement space, where Poisson noise was simulated. The amount of

noise simulates thereby the acquisition time. In a final step, the sinograms were reconstructed[2] with an EM algorithm [33, 34].

## 2.5 Hardware Phantom Data

Two cardiac phases, diastole and systole, with additional different respiratory phase were simulated with a custom made thorax phantom including a commercially available hardware heart phantom (BS Industrieelektronik & Medizintechnik, Germany) [51]. The myocardium of the hardware phantom consists of a flexible double-membrane that can be filled with radioactive water to simulate the left ventricular myocardium. Cardiac motion is simulated by pumping water into the inner cavity using a pneumatic system (diastole) and by releasing the pressure (systole). Respiratory motion is simulated with an elastic membrane, fixed at the position of the diaphragm, which can be moved in and out by a pneumatically driven device.

A 3 minute static list mode PET scan was performed for each phase on the scanner described in Section 2.6. Besides using the full 3 minutes scan, the list mode files were additionally cropped to 7.2 seconds (same time as a single gate in the 3 minutes patient scans) to demonstrate the performance of our methods on data with low statistics. The images have a total size of $175 \times 175 \times 47$ with a voxel size of 3.375 mm. The heart of the phantom was filled with $^{18}$F-FDG (208.6 kBq/mL). The rest of the phantom body was filled with some background activity (9.2 kBq/mL). The data was decay-corrected after acquisition. In addition, a CT scan was performed for each of the two heart phases, serving as a morphological reference. The CT scans were performed directly after the respective PET acquisitions to achieve an optimal alignment.

## 2.6 Patient Data

Data of 21 patients (19 male, 2 female; between 37 and 76 years old) with known coronary artery disease was acquired and used for cardiac and respiratory motion correction after gating. One hour after injection of $^{18}$F-FDG (4 MBq/kg) a 20 minute list mode scan was acquired for evaluation of myocardial viability prior to revascularization. All patients underwent a hyperinsulinemic euglycemic clamp technique before and during the scan to enhance FDG uptake in the heart. In addition $\beta$-blockers were administered to all patients to lower and keep constant the heart rate during examination.

Besides using the full 20 minutes scan, the list mode files were additionally cropped to 3 minutes to demonstrate the performance of our methods on data with low statistics.

All scans were performed on a Siemens Biograph$^{\text{TM}}$ Sensation 16 PET/CT scanner (Siemens Medical Solution) with a spatial resolution of around $6 - 7$ mm

[2] With a Gaussian smoothing of $R_{rec} = 4$ mm FWHM during reconstruction, this results in a final resolution of $R_{fin} \approx \sqrt{R_{sys}^2 + R_{rec}^2} \approx 5.55$ mm. This is the theoretical maximal resolution. In practice, a resolution of around $6 - 7$ mm was detected [19] ($R_{rec} = 5$ mm).

[19]. During list mode acquisition an ECG signal was recorded for cardiac gating.

Image reconstruction was performed with a 3D EM software EMrecon [33, 34]. The implementation is based on the standard MLEM [56] and OS-MLEM [25] methods. 20 iterations with one subset were chosen. The output images are sampled with $175 \times 175 \times 47$. Given an isotropic voxel size of 3.375 mm, this results in a field of view (FOV) of $590.625\,\text{mm} \times 590.625\,\text{mm} \times 158.625\,\text{mm}$. To prevent the attenuation correction artifacts discussed above, cf. [15], motion correction was performed on data that was not corrected for attenuation during reconstruction.

## 2.7 Dual gating of patient data in thoracic PET

In pure respiratory gated PET, each gate still contains cardiac motion. Analogously, pure cardiac gated PET images still contain respiratory motion. Hence, we make use of dual gating to further reduce the amount of motion contained in the images [43, 57, 32, 37, 30]. In dual gating, a $n \times m$ matrix of $n$ cardiac and $m$ respiratory images is built, i.e., each cardiac phase is over again divided into all respiratory phases (or vice versa) (see Fig. 8). The number of gates was set to $m = n = 5$ for all computations in this paper. Consequently, time information about cardiac and respiratory motion is required. Information about the cardiac cycle was provided by an ECG signal. The cardiac cycle was divided into equidistant intervals. The respiratory signals were estimated on basis of list mode data without auxiliary measurements [11]. To this end, the list mode stream is divided in 50-ms frames with subsequent computation of the axial center of mass along the scanner axis of the measured counting rates in the respective frames. Amplitude based gating was applied to the respiratory signal, deduced from changes in the center of mass. According to this information both, the 20 minutes and the 3 minutes, list mode files of the PET acquisitions are divided into dual (cardiac and respiratory) gates yielding individual reconstructions. For a more detailed explanation we refer to [43].

## 2.8 Choice of regularization parameters

We propose an XCAT based selection method to determine the three weighting factors $\alpha_l$, $\alpha_a$, and $\alpha_v$ in hyperelastic regularization (7). To this end, the output of the XCAT phantom was processed to resemble the patient scans in terms of tracer distribution, noise, and the scanning system (see Section 2.4). Thus, we can determine a good parameter set utilizing the ground-truth motion vectors $y_{GT}$, that are used by the XCAT phantom for the generation of the data. For any estimated transformation $y$ the deviation from $y_{GT}$ can be computed with quantitative measures. We use the error measure $e$ [6] to quantify the deviation

$$e(y, y_{GT}) := \frac{1}{|\Omega|} \int_\Omega \|y(x) - y_{GT}(x)\| dx \,. \tag{12}$$

The parameter set $\{\tilde{\alpha_l}, \tilde{\alpha_a}, \tilde{\alpha_v}\}$ that minimizes $e$ is optimal:

$$\{\tilde{\alpha_l}, \tilde{\alpha_a}, \tilde{\alpha_v}\} = \arg\min \{e(\tilde{y}(\alpha_l, \alpha_a, \alpha_v),\ y_{GT}) \mid \alpha_l, \alpha_a, \alpha_v \in [0, 30]\}\ , \tag{13}$$

where for each parameter set the optimal deformation $\tilde{y}(\alpha_l, \alpha_a, \alpha_v)$ is computed by

$$\begin{aligned} \tilde{y}(\alpha_l, \alpha_a, \alpha_v) &:= \arg\min_y\ \mathcal{D}(\mathcal{M}^{\mathrm{MP}}(\mathcal{T}, y),\ \mathcal{R}) \\ &+ \mathcal{S}^{\mathrm{hyper}}(y, \alpha_l, \alpha_a, \alpha_v)\ . \end{aligned} \tag{14}$$

## 2.9 Evaluation

For validation of the phantom data we make use of the ground-truth deformation vectors provided by the XCAT phantom. In addition, intensity, transformation and contour based criteria are applied for evaluation. For patient data only the intensity, transformation and contour based methods can be applied, as no ground-truth information of the displacement is available.

### 2.9.1 Comparison with ground-truth vectors

For the XCAT phantom, the estimated deformations are compared to the known deformations by the error measure $e$ defined in (12). Further, the maximum deformation

$$\mathrm{e}^{\max}(y, y_{GT}) := \max_{x \in \Omega} \|y(x) - y_{GT}(x)\| \tag{15}$$

is analyzed to assure that no unphysiologically large deformations occur. The relative error RE specifies the improvement of $y$ according to $e$ in reference to the identity transformation $y_{ref}$

$$\mathrm{RE}(y, y_{GT}) := \frac{e(y, y_{GT})}{e(y_{ref}, y_{GT})}\ . \tag{16}$$

This allows to measure the improvement compared to the distance before registration.

### 2.9.2 Normalized Cross-Correlation (NCC)

The widely used NCC will be applied as an intensity based criterion.

**Definition 4 (NCC)** *For two images $\mathcal{T}$ and $\mathcal{R}$ the* normalized cross-correlation *(NCC) is defined as*

$$\mathrm{NCC}(\mathcal{T}, \mathcal{R}) := \frac{\langle \mathcal{T}_u, \mathcal{R}_u \rangle}{\|\mathcal{T}_u\|\, \|\mathcal{R}_u\|}\ . \tag{17}$$

*where $\mathcal{T}_u = \mathcal{T} - \mu(\mathcal{T})$ and $\mathcal{R}_u = \mathcal{R} - \mu(\mathcal{R})$ are the unbiased versions of $\mathcal{T}$ and $\mathcal{R}$. For an image $I$, $\mu(I)$ is the expected value.*

#### 2.9.3 Center of Mass (COM)

To evaluate the correction of motion induced by translation of the heart's center, the heart's shift is examined [15]. To this end, the heart is segmented with an expert selected threshold and the center of mass is computed for each gate. The difference of the center of mass with regard to the reference gate indicates the heart's displacement.

As all gates of the 20 minutes scan contain enough statistics, a threshold based segmentation is practicable. In contrast, the gates of the 3 minutes patient scans are too noisy to make this evaluation applicable.

#### 2.9.4 Range of the Jacobian map

The transformation's regularity is analyzed via the range of the Jacobian map. Controlling the maximum decrease or increase of a voxel's volume or intensity, orientation preserving and diffeomorphic transformations, i.e., free of foldings, can be assured. Accordingly, dropping the absolute value bars in (4) is justified.

# 3 Results

We evaluate our mass-preserving registration framework VAMPIRE on phantom and patient data. In Section 3.1, the performance of our method is evaluated quantitatively based on the ground-truth deformation field provided by the XCAT software phantom. In Section 3.2, the hardware phantom serves as a validation under clinical conditions with additional CT images.

In Section 3.3, the applicability to dual gated patient data is demonstrated on basis of the whole 20 minutes scans. Data with a reduced statistic of 3 minutes is evaluated in Section 3.4.

## 3.1 XCAT Software Phantom

A parameter search was performed on the XCAT data to find an adequate set of regularization parameters $\alpha_l$, $\alpha_a$, and $\alpha_v$ according to (13). As our data simulates specific heart scans with uptake almost exclusively in the left ventricle, the ground-truth vector comparison was restricted to the left ventricle. With a four-level pyramid in our multi-resolution framework ($22 \times 22 \times 6$, $44 \times 44 \times 12$, $88 \times 88 \times 24$, and $175 \times 175 \times 47$) we found the following optimal parameters:

$$\alpha_l = 5 \ , \quad \alpha_a = 1 \ , \quad \alpha_v = 10 \ . \tag{18}$$

The registration result for the male XCAT data using the optimal parameters is depicted in Fig. 3. The image in (c), showing a slice of the heart in systole and maximum inspiration, is registered to the reference image in (a), showing the heart in diastole and mid-expiration. The registration result with VAMPIRE is shown in (e). The estimated transformation $y$ is represented by the superimposed grid in (c). A comparison of $y$ (red arrows) and the ground-truth vectors $y_{GT}$ (blue arrows) can be seen in (g) for the male anatomy.

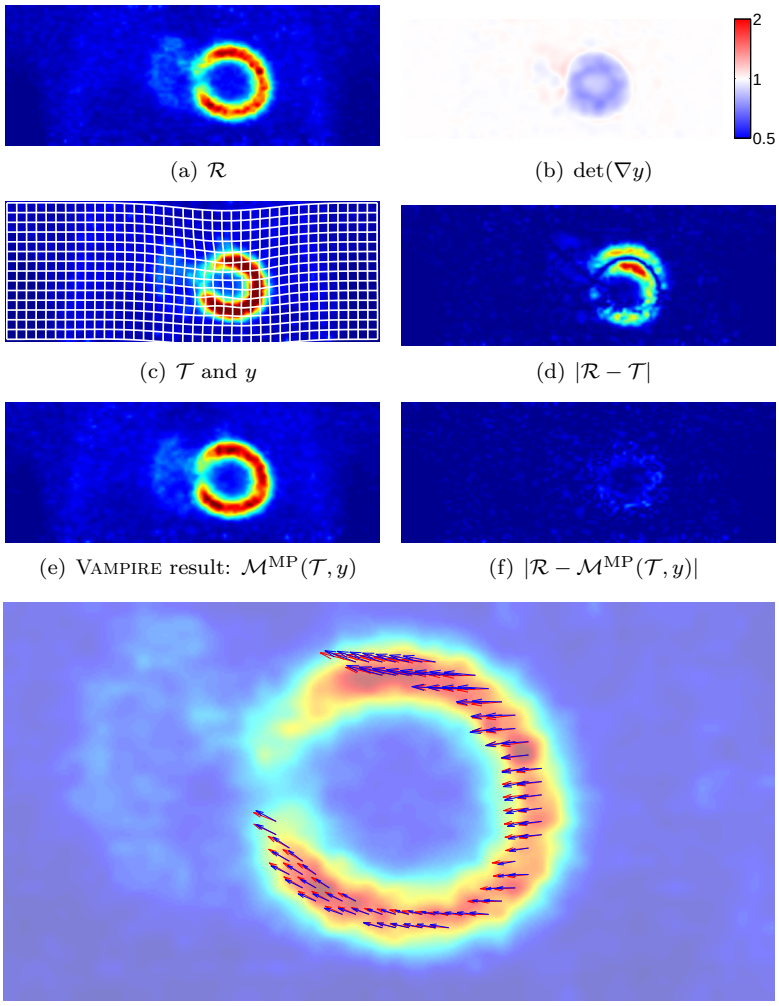


(a) $\mathcal{R}$ (b) $\det(\nabla y)$

(c) $\mathcal{T}$ and $y$ (d) $|\mathcal{R} - \mathcal{T}|$

(e) VAMPIRE result: $\mathcal{M}^{\mathrm{MP}}(\mathcal{T}, y)$ (f) $|\mathcal{R} - \mathcal{M}^{\mathrm{MP}}(\mathcal{T}, y)|$

(g) $\mathcal{R}$ with ground-truth $y_{GT}$ (blue) and estimated vectors $y$ (red).

Figure 3: Motion correction of the XCAT software phantom data (coronal slices). $\mathcal{T}$ (c) is registered to $\mathcal{R}$ (a) using VAMPIRE resulting in (e). The absolute difference images before (d) and after motion correction (f) illustrate the accuracy. The estimated transformation $y$ (c) is smooth and invertible which is further demonstrated with the Jacobian map (b). The logarithmic color map ranges from 0.5 (blue) over 1 (white) to 2 (red). The ground-truth comparison (restricted to the left ventricle; male anatomy) can be seen in (g).

An average error according to (12) of 1.624 mm and a maximum error of

Table 1: Evaluation of the XCAT phantom results in a region around the heart. The transformation $y$ estimated with VAMPIRE is compared to the ground-truth transformation $y_{GT}$. An evaluation of the VAMPIRE result $\mathcal{M}^{\mathrm{MP}}(\mathcal{T}, y)$ is given on image basis using NCC for both XCAT anatomies.

| | XCAT (male) | XCAT (female) |
|---|---|---|
| $e(y, y_{GT})$ | 1.624 mm | 1.965 mm |
| $\mathrm{e}^{\max}(y, y_{GT})$ | 3.863 mm | 4.086 mm |
| $\mathrm{RE}(y, y_{GT})$ | 0.162 | 0.192 |
| $\min_x\{\det(\nabla y(x))\}$ | 0.677 | 0.671 |
| $\max_x\{\det(\nabla y(x))\}$ | 1.168 | 1.301 |
| $\mathrm{NCC}(\mathcal{T}, \mathcal{R})$ | 0.823 | 0.827 |
| $\mathrm{NCC}(\mathcal{M}^{\mathrm{MP}}(\mathcal{T}, y), \mathcal{R})$ | 0.971 | 0.978 |

3.863 mm (see (15)) could be achieved, given a voxel size of 3.375 mm. The range of the Jacobian map is $[0.677, 1.168]$. Comparing $\mathcal{T}$ and our result $\mathcal{M}^{\mathrm{MP}}(\mathcal{T}, y)$ with $\mathcal{R}$, the NCC increased from 0.823 before to 0.971 after registration, cf. Fig. 3(d) and (f).

In practice, noise corrupts the images and obtaining the maximum correlation value 1 would indicate an overfitting of $y$. Thus, we reconstructed a second version $\bar{\mathcal{R}}$ of the reference image for comparison. $\bar{\mathcal{R}}$ differs from $\mathcal{R}$ only in the random Poisson noise (the same amount of noise was applied to both images). Thus, $\mathrm{NCC}(\mathcal{R}, \bar{\mathcal{R}}) = 0.969$ represents the aimed correlation value. With our method we achieved almost exactly this correlation, i.e., $\mathrm{NCC}(\mathcal{M}^{\mathrm{MP}}(\mathcal{T}, y), \mathcal{R}) = 0.971$, which indicates that no overfitting occurs. The quantitative measures for the XCAT data are summarized in Tab. 1 (for the male and female anatomy). The time for registration of the two XCAT phantom gates was 4 min 46 s. The number of iterations for the different levels are 4, 3, 2, and 2, starting from the lowest resolution.

## 3.2 Hardware Phantom

The hardware phantom was evaluated in a high (3 minutes) and low (7.2 seconds) statistic version. Each image was cropped to a region of $100 \times 88 \times 44$ voxel containing the whole body. The four levels for the registration are $13 \times 11 \times 6$, $25 \times 22 \times 11$, $50 \times 44 \times 22$, and $100 \times 88 \times 44$.

### 3.2.1 3 Minutes Scan

We found empirically that $\alpha_l = 50$, $\alpha_a = 10$, and $\alpha_v = 100$ is a good choice for the regularization parameters of the 3 minutes hardware phantom scan. The

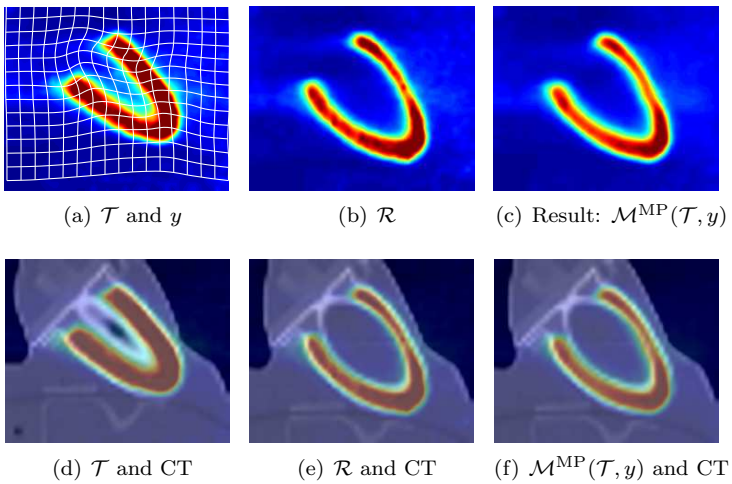

(a) $\mathcal{T}$ and $y$ (b) $\mathcal{R}$ (c) Result: $\mathcal{M}^{\mathrm{MP}}(\mathcal{T}, y)$

(d) $\mathcal{T}$ and CT (e) $\mathcal{R}$ and CT (f) $\mathcal{M}^{\mathrm{MP}}(\mathcal{T}, y)$ and CT

Figure 4: Cardiac motion correction of hardware phantom data (3 minutes scans). $\mathcal{T}$ (a) is registered to $\mathcal{R}$ (b) using VAMPIRE resulting in (c). An overlay of $\mathcal{T}$, $\mathcal{R}$, and $\mathcal{M}^{\mathrm{MP}}(\mathcal{T}, y)$ with their respective CT scans can be seen in (d), (e), and (f).

registration results are shown in Fig. 4. In (a), $\mathcal{T}$ together with the estimated transformation grid $y$ is illustrated. The image in (b) served as reference $\mathcal{R}$. After applying $y$ to $\mathcal{T}$ with subsequent intensity modulation, the image in (c) results. An overlay of $\mathcal{T}$ and the respective CT image is shown in (d). An analogous overlay for $\mathcal{R}$ and our result can be seen in (e) respectively (f). The NCC between $\mathcal{T}$ and $\mathcal{R}$ is 0.552 and increased to 0.985 after registration. With $[0.479, 1.375]$, the range of the Jacobian assures that the estimated transformation is free of foldings. The registration process took 1 min 6 s. The algorithm converged after 4, 4, 4, and 3 iterations on the respective levels.

#### 3.2.2 7.2 Seconds Scan

For the 7.2 seconds scan we found empirically that $\alpha_l = 100$, $\alpha_a = 10$, and $\alpha_v = 50$ is a good choice for the regularization parameters. An analogue representation of the registration results as in Fig. 4 is given in Fig. 5 for the 7.2 seconds scan. The NCC between $\mathcal{T}$ and $\mathcal{R}$ is 0.537 and increased to 0.952 after registration. With $[0.405, 1.284]$, the range of the Jacobian assures that the estimated transformation is free of foldings. The registration process took 2 min 13 s. The algorithm converged after 4, 3, 5, and 2 iterations on the respective levels. The results for both statistics are summarized in Tab. 2.

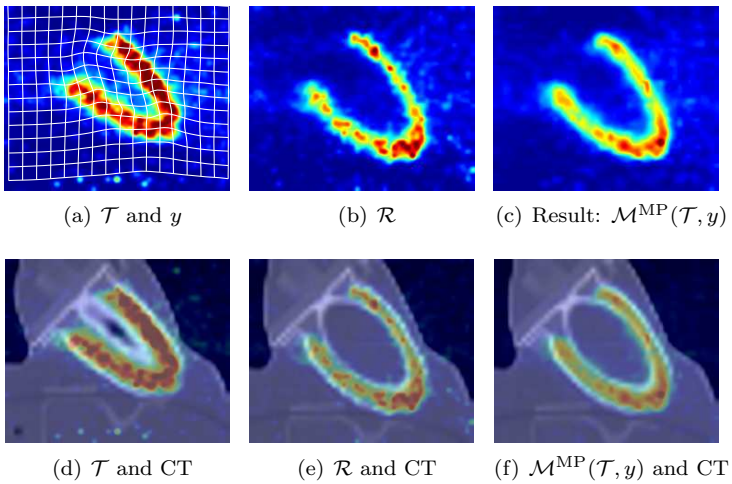

(a) $\mathcal{T}$ and $y$ (b) $\mathcal{R}$ (c) Result: $\mathcal{M}^{\mathrm{MP}}(\mathcal{T}, y)$

(d) $\mathcal{T}$ and CT (e) $\mathcal{R}$ and CT (f) $\mathcal{M}^{\mathrm{MP}}(\mathcal{T}, y)$ and CT

Figure 5: Cardiac motion correction of hardware phantom data (7.2 seconds scans). $\mathcal{T}$ (a) is registered to $\mathcal{R}$ (b) using VAMPIRE resulting in (c). An overlay of $\mathcal{T}$, $\mathcal{R}$, and $\mathcal{M}^{\mathrm{MP}}(\mathcal{T}, y)$ with their respective CT scans can be seen in (d), (e), and (f).

Table 2: Evaluation of the hardware phantom results in a region around the heart. An evaluation of the VAMPIRE result $\mathcal{M}^{\mathrm{MP}}(\mathcal{T}, y)$ is given on image basis using NCC for both statistics.

| | Hardware Phantom (3 minutes scan) | Hardware Phantom (7.2 seconds scan) |
|---|---|---|
| $\min_x\{\det(\nabla y(x))\}$ | 0.479 | 0.405 |
| $\max_x\{\det(\nabla y(x))\}$ | 1.375 | 1.284 |
| $\mathrm{NCC}(\mathcal{T}, \mathcal{R})$ | 0.552 | 0.537 |
| $\mathrm{NCC}(\mathcal{M}^{\mathrm{MP}}(\mathcal{T}, y), \mathcal{R})$ | 0.985 | 0.952 |

### 3.3 Patient study (20 minutes scans)

For each of the 21 patients dual gating was performed with five respiratory and five cardiac gates. The gate representing mid-expiration and the diastole was chosen as reference $\mathcal{R}$ as the heart is most of the time in diastole and as the mid-expiration phase shows the smallest deformation (caused by respiration) to the other gates on average.

Each of the 24 template images was registered to the reference image using VAMPIRE. We use the determined regularization parameters from Section 3.1, i.e., $\alpha_l = 5$, $\alpha_a = 1$, and $\alpha_v = 10$. For registration the images were cropped to

the region containing the patient resulting in a multi-level pyramid of $16 \times 13 \times 6$, $32 \times 25 \times 11$, $64 \times 50 \times 22$, and $128 \times 100 \times 44$.

For one patient and one gate we illustrate our results in Fig. 6 with coronal slices. For the template gate in Fig. 6(c) we chose the systolic heart phase in maximum inspiration, which has maximum displacement compared to the reference gate (a) in diastole and mid-expiration and is thus the most challenging gate. The estimated transformation $y$ is overlaid in (c). In (f), the absolute difference image of $\mathcal{R}$ and the resulting image $\mathcal{M}^{\mathrm{MP}}(\mathcal{T}, y)$ of our method (e) is shown. For better comparability, we added our final result (average image) (g) and the uncorrected image (h) from Fig. 1.

As described in Section 2.6, all patients suffer from coronary artery disease. The patient images shown in this Section contain a defect at the inferior wall. The slice shown for the XCAT phantom (Fig. 3(a)) and for the patient data (Fig. 6(a)) is comparable (coronal slice through the hearts center). To illustrate the exact location of the infarction, we marked the region of scar tissue in these two slices in Fig. 7.

As no ground-truth information for the patient data is available and as good matches based on image data alone do not implicitly guarantee meaningful underlying transformations, the performance of our method is evaluated with image and transformation based methods. For validation based on the transformation, the range of the Jacobian map and the maximum deformation is analyzed. The minimum of all Jacobian maps (all patients and all gates) is 0.340 and the maximum is 2.375, i.e., no negative or too large values appear. The maximum deformation across all patients is 23.29 mm. We further visualize the performance of our method by plotting a coronal slice of the estimated transformations for each gate underlaid with the corresponding template image in Fig. 8. Additional difference images of the same coronal slice are shown in Fig. 9 to provide a voxel-by-voxel comparison of the reference image and the transformed template images.

The image based measures are NCC and COM. On average the NCC for all patients and all gates increased from $0.878 \pm 0.066$ to $0.972 \pm 0.002$. For the most challenging gates in relation to the reference gate, i.e., heart in systole and heart in maximum inspiration, we found an increase from $0.804 \pm 0.056$ to $0.968 \pm 0.001$ and $0.793 \pm 0.060$ to $0.970 \pm 0.002$, respectively. We also quantitatively compared the bottom-line output image (Fig. 6(g)) with the reference image (Fig. 6(a)) resulting in an NCC value of 0.985. The results for the NCC comparison are given in more detail in Tab. 3. Further, the upper row of Fig. 10 illustrates the average values from the last row and column of Tab. 3. Analyzing the COM, the heart's shift could be reduced significantly from $5.809 \pm 3.413$ mm to $0.723 \pm 0.212$ mm as well. Detailed results for the COM comparison are given

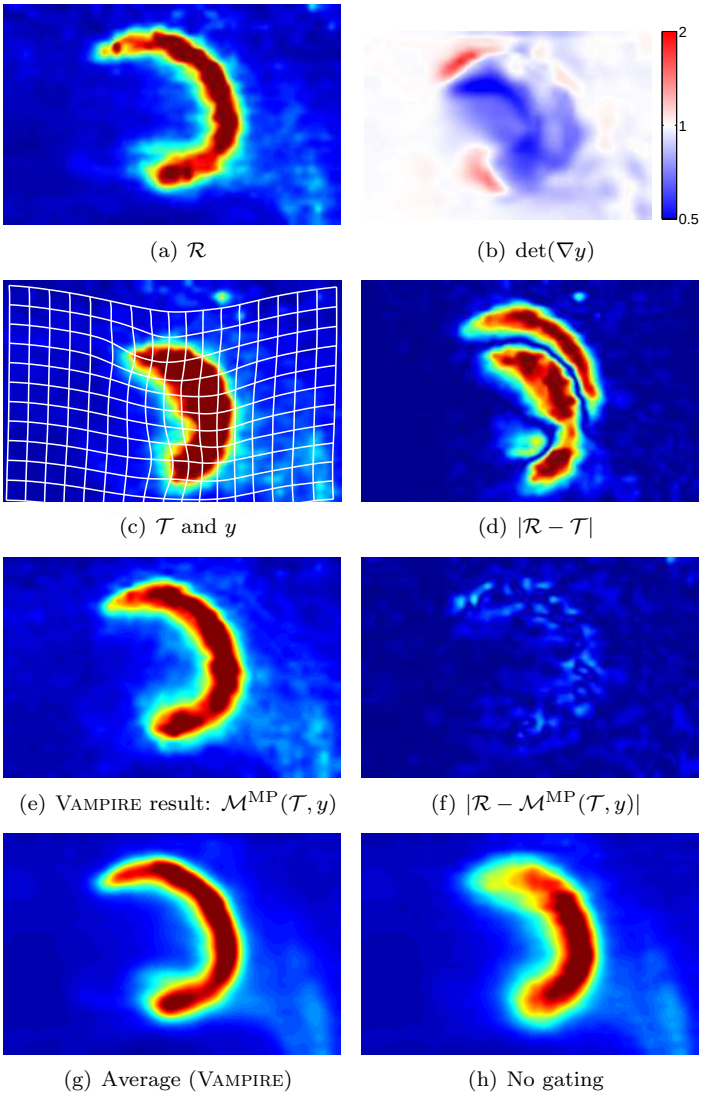


(a) $\mathcal{R}$ (b) $\det(\nabla y)$

(c) $\mathcal{T}$ and $y$ (d) $|\mathcal{R} - \mathcal{T}|$

(e) VAMPIRE result: $\mathcal{M}^{\mathrm{MP}}(\mathcal{T}, y)$ (f) $|\mathcal{R} - \mathcal{M}^{\mathrm{MP}}(\mathcal{T}, y)|$

(g) Average (VAMPIRE) (h) No gating

Figure 6: Motion correction of the patient data for one patient exemplary (20 minutes scan). $\mathcal{T}$ (c) is registered to $\mathcal{R}$ (a) using VAMPIRE resulting in (e). The absolute difference image before (d) and after motion correction (f) illustrate the accuracy. The estimated transformation $y$ (c) is smooth and free of foldings which can also be seen at the plot of the Jacobian map (b). The logarithmic color map ranges from 0.5 (blue) over 1 (white) to 2 (red).

in Tab. 4 and the lower row of Fig. 10.

To measure the preservation of intensity, the total volume intensity in the

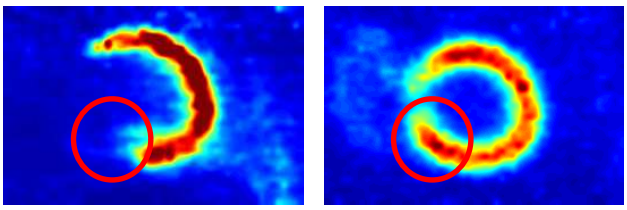

(a) Patient (b) XCAT

Figure 7: The coronal slice in (a) is taken from the patient data in Fig. 6(a). It is known that the patient has scar tissue at the inferior wall due to coronary artery disease. The comparable coronal slice in (b), taken from the XCAT phantom (cf. Fig. 3(a)), illustrates how a healthy heart would look like in that region.

Table 3: NCC of the human data (20 minutes scans) evaluated in a rectangular region around the heart. Res. 1 is the respiratory phase of maximum expiration, and Res. 5 of maximum inspiration. Car. 2 represents the systole and Car. 5 the diastole. The last row and column show average values.

NCC before motion correction:

| | Res. 1 | Res. 2 | Res. 3 | Res. 4 | Res. 5 | Avg. |
|---|---|---|---|---|---|---|
| Car. 1 | 0.898 | 0.898 | 0.883 | 0.847 | 0.752 | 0.855 |
| Car. 2 | 0.848 | 0.841 | 0.827 | 0.791 | 0.712 | 0.804 |
| Car. 3 | 0.924 | 0.937 | 0.936 | 0.907 | 0.813 | 0.903 |
| Car. 4 | 0.925 | 0.948 | 0.955 | 0.933 | 0.841 | 0.920 |
| Car. 5 | 0.921 | 0.949 | $\mathcal{R}$ | 0.943 | 0.850 | 0.916 |
| Avg. | 0.903 | 0.915 | 0.900 | 0.884 | 0.793 | |

NCC after motion correction:

| | Res. 1 | Res. 2 | Res. 3 | Res. 4 | Res. 5 | Avg. |
|---|---|---|---|---|---|---|
| Car. 1 | 0.971 | 0.972 | 0.972 | 0.972 | 0.969 | 0.971 |
| Car. 2 | 0.968 | 0.969 | 0.969 | 0.969 | 0.966 | 0.968 |
| Car. 3 | 0.973 | 0.973 | 0.973 | 0.973 | 0.970 | 0.972 |
| Car. 4 | 0.973 | 0.973 | 0.973 | 0.974 | 0.972 | 0.973 |
| Car. 5 | 0.973 | 0.974 | $\mathcal{R}$ | 0.974 | 0.972 | 0.973 |
| Avg. | 0.972 | 0.972 | 0.972 | 0.972 | 0.970 | |

images is compared to the total volume intensity in the transformed images. The summed intensities before transformation are $(7.27 \pm 0.24)10^7$ compared to $(7.24 \pm 0.21)10^7$ after transformation, which indicates the preservation of mass.

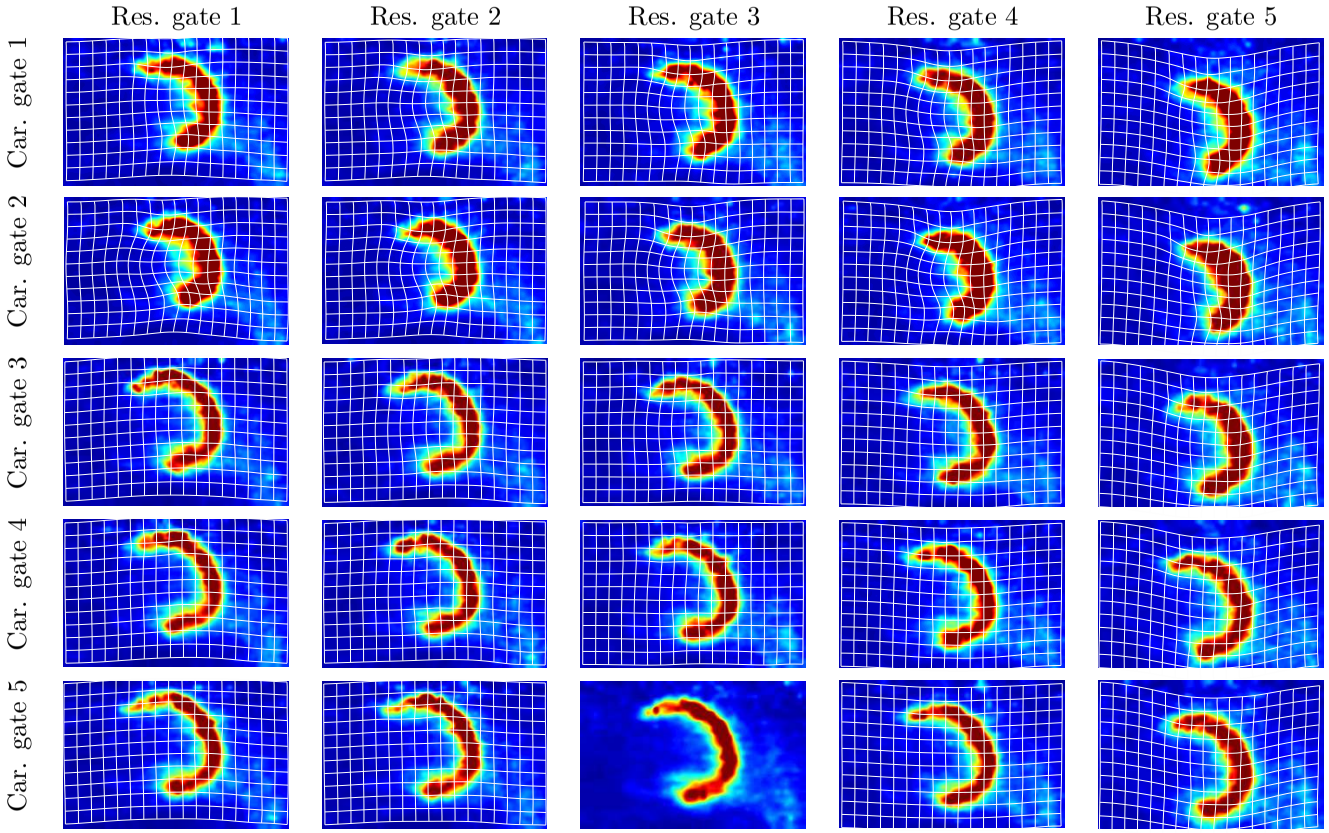


Figure 8: Coronal slices of a human dataset (20 minutes scans) with five respiratory and five cardiac gates are shown with superimposed deformation grids estimated with VAMPIRE. The columns define the respiratory gates and the rows represent the cardiac cycle. The reference gate is in the bottom row and third column without an overlaid grid.

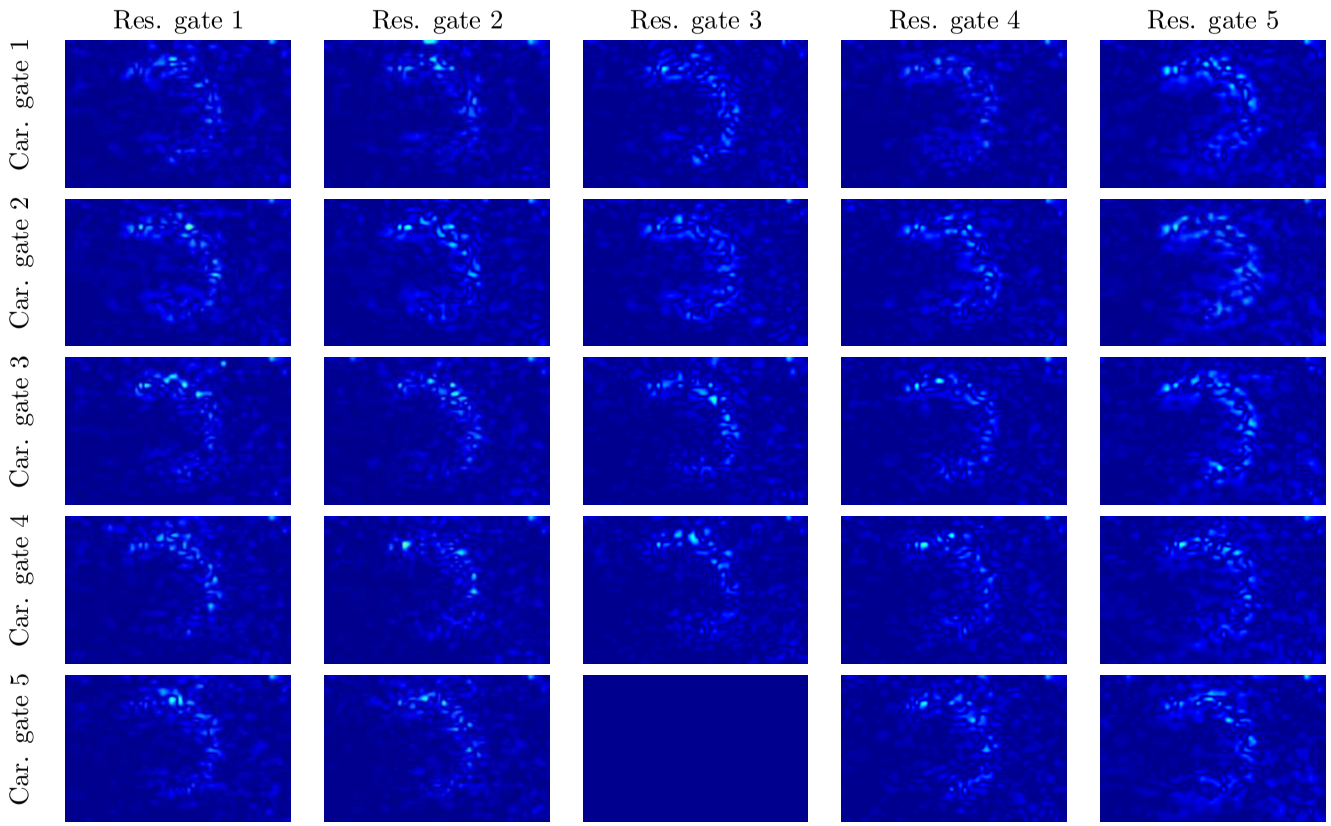


Figure 9: Coronal slices of the difference images $\left(|\mathcal{R} - \mathcal{M}^{\mathrm{MP}}(\mathcal{T}_i, y)|, i \in \{1, \ldots, 25\}\right)$ for one human dataset (20 minutes scans; same patient as in Fig. 8) with five respiratory and five cardiac gates are shown. The columns define the respiratory gates and the rows represent the cardiac cycle. The difference image of the reference gate (i.e. $|\mathcal{R} - \mathcal{R}|$) is the empty image in the bottom row and third column. The intensity scaling is the same as in Fig. 8.

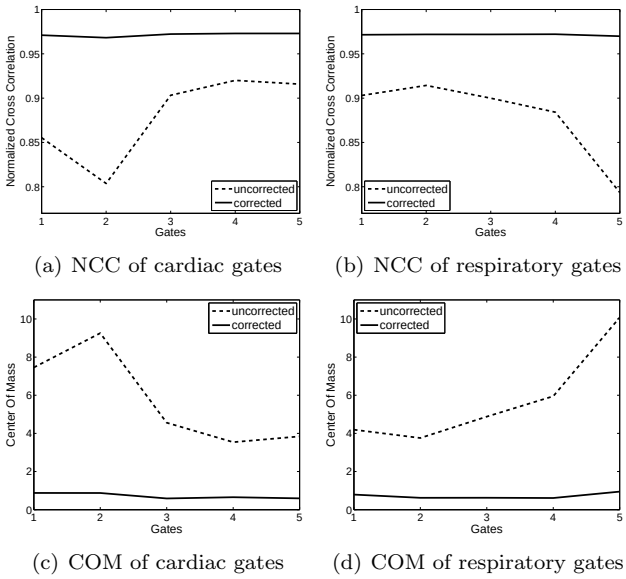


(a) NCC of cardiac gates (b) NCC of respiratory gates

(c) COM of cardiac gates (d) COM of respiratory gates

Figure 10: NCC (upper row, evaluated in a rectangular region around the heart) and COM (lower row) of patient data (20 minutes scans). The average NCC before and after motion correction is plotted for all cardiac (a) and respiratory (b) gates. The average COM before and after motion correction is plotted for all cardiac (c) and respiratory (d) gates.

The registration process for one image took 2 min 31 s on average. The same processing time applies to the 3 minutes scans analyzed in the next section.

## 3.4 Patient study (3 minutes scans)

The scans from Section 3.3 were cropped to 3 minutes and dual gated with five respiratory and five cardiac gates. Hence, each gate is reconstructed from 7.2 seconds of the list mode data.

The regularization parameters were again determined in a parameter search of XCAT data. The noise level of the XCAT data was adjusted to be comparable to an individual gate as described in Section 2.4. We found that $\alpha_l = 10$, $\alpha_a = 1$, and $\alpha_v = 5$ are the optimal parameters for this noise level. For registration the images were cropped to a size of $128 \times 100 \times 44$. The resulting image sizes in the multi-level pyramid are $16 \times 13 \times 6$, $32 \times 25 \times 11$, $64 \times 50 \times 22$, and $128 \times 100 \times 44$.

For the patient in Fig. 6, we show our results based on the 3 minutes data in Fig. 11. The template gate (c) shows the systolic heart phase in maximum inspiration and the reference gate (a) the diastole and mid-expiration. The estimated transformation $y$ is overlaid in (c). The absolute difference image

Table 4: COM of the human data (20 minutes scans). Res. 1 is the respiratory phase of maximum expiration, and Res. 5 of maximum inspiration. Car. 2 represents the systole and Car. 5 the diastole. The last row and column show average values.

COM before motion correction:

| | Res. 1 | Res. 2 | Res. 3 | Res. 4 | Res. 5 | Avg. |
|---|---|---|---|---|---|---|
| Car. 1 | 4.912 | 5.359 | 6.489 | 8.311 | 12.211 | 7.456 |
| Car. 2 | 6.585 | 7.197 | 8.332 | 10.251 | 13.917 | 9.257 |
| Car. 3 | 2.598 | 2.402 | 3.115 | 5.200 | 9.479 | 4.559 |
| Car. 4 | 2.954 | 1.759 | 1.582 | 3.571 | 7.833 | 3.540 |
| Car. 5 | 3.921 | 2.084 | $\mathcal{R}$ | 2.411 | 6.950 | 3.842 |
| Avg. | 4.194 | 3.760 | 4.880 | 5.949 | 10.078 | |

COM after motion correction:

| | Res. 1 | Res. 2 | Res. 3 | Res. 4 | Res. 5 | Avg. |
|---|---|---|---|---|---|---|
| Car. 1 | 1.044 | 0.649 | 0.892 | 0.711 | 1.093 | 0.878 |
| Car. 2 | 0.760 | 0.939 | 0.663 | 0.849 | 1.164 | 0.875 |
| Car. 3 | 0.657 | 0.457 | 0.489 | 0.552 | 0.791 | 0.589 |
| Car. 4 | 0.844 | 0.519 | 0.465 | 0.507 | 0.949 | 0.656 |
| Car. 5 | 0.651 | 0.548 | $\mathcal{R}$ | 0.442 | 0.736 | 0.594 |
| Avg. | 0.791 | 0.622 | 0.627 | 0.612 | 0.946 | |

of $\mathcal{R}$ and $\mathcal{T}$ (d) respectively the resulting image $\mathcal{M}^{\mathrm{MP}}(\mathcal{T}, y)$ (f) after applying our method is shown. The final resulting image after averaging of all aligned images (g) has to be compared to the image without any corrections (h).

We analyze the NCC and Jacobian range whereas the COM measure is not applicable to this data, as a threshold based segmentation of such noisy data is not accurate enough. On average the NCC for all patients and all gates increased from $0.689 \pm 0.052$ to $0.803 \pm 0.002$. For the most challenging gates in relation to the reference gate, i.e., heart in systole and heart in maximum inspiration, we found an increase from $0.624 \pm 0.043$ to $0.801 \pm 0.002$ and $0.623 \pm 0.045$ to $0.801 \pm 0.002$, respectively. The quantitative comparison of the bottom-line output image (Fig. 11(g)) and the reference image (Fig. 11(a)) provides an NCC value of 0.891. Plots showing the average NCC values for all respiratory and cardiac gates are presented in Fig. 12. Note that the upper limit of the y-axis is not set to 1 to improve the readability. The average NCC value across all patients is shown for each individual gate in Tab. 5. The Jacobian map among

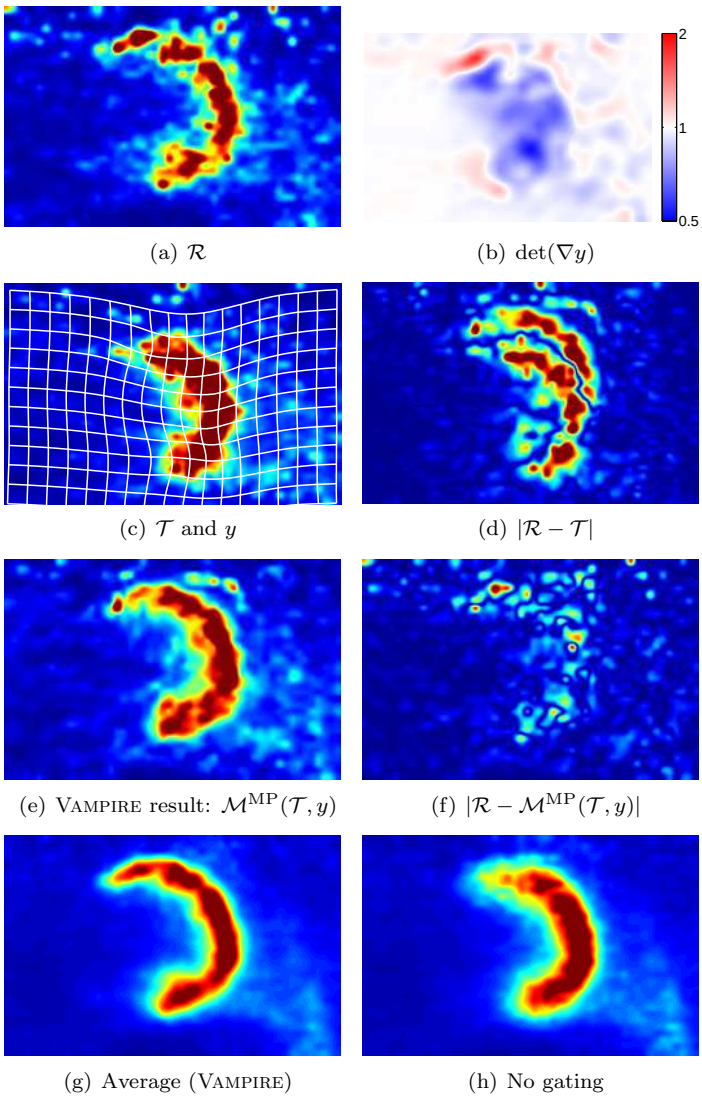


(a) $\mathcal{R}$ (b) $\det(\nabla y)$

(c) $\mathcal{T}$ and $y$ (d) $|\mathcal{R} - \mathcal{T}|$

(e) VAMPIRE result: $\mathcal{M}^{\mathrm{MP}}(\mathcal{T}, y)$ (f) $|\mathcal{R} - \mathcal{M}^{\mathrm{MP}}(\mathcal{T}, y)|$

(g) Average (VAMPIRE) (h) No gating

Figure 11: Motion correction of the patient data for one patient exemplary (3 minutes scan). $\mathcal{T}$ (c) is registered to $\mathcal{R}$ (a) using VAMPIRE resulting in (e). The absolute difference image before (d) and after motion correction (f) illustrate the accuracy. The estimated transformation $y$ (c) is smooth and free of foldings which can also be seen at the plot of the Jacobian map (b). The logarithmic color map ranges from 0.5 (blue) over 1 (white) to 2 (red).

all patients and all gates ranges from 0.313 to 2.377.

For the 3 minutes scans, the summed intensities before transformation are

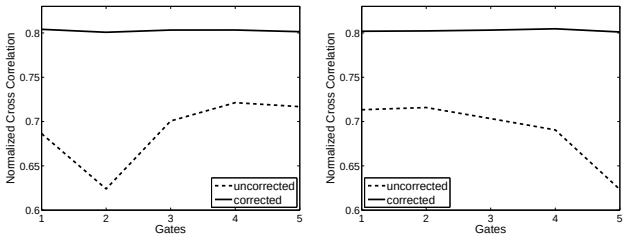


(a) NCC of cardiac gates (b) NCC of respiratory gates

Figure 12: NCC of patient data (3 minutes scans) evaluated in a rectangular region around the heart. The average NCC before and after motion correction is plotted for all cardiac (a) and respiratory (b) gates.

Table 5: NCC of the human data (3 minutes scans) evaluated in a rectangular region around the heart. Res. 1 is the respiratory phase of maximum expiration, and Res. 5 of maximum inspiration. Car. 2 represents the systole and Car. 5 the diastole.

NCC before motion correction:

| | Res. 1 | Res. 2 | Res. 3 | Res. 4 | Res. 5 | Avg. |
|---|---|---|---|---|---|---|
| Car. 1 | 0.717 | 0.716 | 0.709 | 0.682 | 0.608 | 0.686 |
| Car. 2 | 0.661 | 0.651 | 0.641 | 0.614 | 0.554 | 0.624 |
| Car. 3 | 0.726 | 0.727 | 0.721 | 0.697 | 0.632 | 0.701 |
| Car. 4 | 0.737 | 0.744 | 0.743 | 0.726 | 0.657 | 0.721 |
| Car. 5 | 0.725 | 0.741 | $\mathcal{R}$ | 0.734 | 0.667 | 0.717 |
| Avg. | 0.713 | 0.716 | 0.703 | 0.691 | 0.623 | |

NCC after motion correction:

| | Res. 1 | Res. 2 | Res. 3 | Res. 4 | Res. 5 | Avg. |
|---|---|---|---|---|---|---|
| Car. 1 | 0.803 | 0.803 | 0.805 | 0.807 | 0.804 | 0.804 |
| Car. 2 | 0.800 | 0.801 | 0.802 | 0.802 | 0.801 | 0.801 |
| Car. 3 | 0.804 | 0.803 | 0.803 | 0.805 | 0.803 | 0.803 |
| Car. 4 | 0.804 | 0.803 | 0.802 | 0.806 | 0.803 | 0.803 |
| Car. 5 | 0.799 | 0.802 | $\mathcal{R}$ | 0.804 | 0.801 | 0.801 |
| Avg. | 0.802 | 0.802 | 0.803 | 0.805 | 0.801 | |

$(8.03 \pm 0.23)10^7$ and after transformation $(7.99 \pm 0.21)10^7$, which again indicates the preservation of mass.

### 3.5 Grid evaluation

A direct comparison of the estimated deformation grids from the 20 minutes scans and 3 minutes scans was performed to analyze the robustness of our method against noise. The motion estimates of the 20 minutes scans serve as a reference as the data contains only few noise.

The grids of corresponding gates were compared according to (12) between the different studies. The mean difference across all patients is 0.725 mm. The range of the Jacobian among all patients and all gates is similar (3 minutes: $[0.313, 2.377]$, 20 minutes: $([0.340, 2.375])$. A maximum deformation of 20.97 mm across all patients for the 3 minutes scans is a bit lower compared to 23.29 mm in the 20 minutes scans, but the deviation of 2.32 mm between the two scans is still below the spatial resolution.

## 4 Discussion and Conclusion

The aim of this paper is the reduction of both cardiac and respiratory motion in thoracic dual gated PET without a loss of statistic. To this end, we presented the novel registration algorithm VAMPIRE that directly incorporates prior knowledge about the mass-preserving property of PET. Although several dual gating approaches exist for motion reduction in PET [43, 31, 29, 57, 32, 37, 30], the motion estimation was so far limited to either cardiac [31, 29] or respiratory [43] motion. VAMPIRE gives, to the best of our knowledge, the first example of a dual motion correction approach with verified effectiveness at cardiac imaging by means of image registration and subsequent averaging. It should be noted, that the focus of this work is not on developing an optimal dual gating scheme, but on the registration based correction of motion in a dual gating setup. Further attempts to improve the dual gating scheme with time varying cardiac gates [57] or grouping of cardiac phases [30] will be considered in future work. In this context, also the optimal number of gates for dual gating needs to be further explored.

Based on the XCAT software phantom data we showed that VAMPIRE yields highly realistic motion estimates with subvoxel accuracy and a very fast convergence. This was quantitatively supported by a comparison with the ground-truth deformation field. The range of the Jacobian map indicates that no foldings or unnatural volumetric changes occur, cf. Fig. 3(b). The robustness against anatomical variations was shown based on a comparison between the male and female anatomy, where comparable good results could be achieved, cf. Tab. 1. As the focus of this work is on the correction of motion induced artifacts only, we did not make use of sophisticated Monte Carlo simulation tools that model effects like scatter or random coincidences. During the determination of the regularization parameters we could detect a certain insensitivity of the exact parameter choice. A plateau around the optimal parameters with similar accuracies could be observed. A certain tolerance in the choice of parameters is therefore given.

The positive results of the software phantom are carried over to real patient data via a hardware phantom validation under realistic conditions where high correlation values could be obtained. The robustness of our method against noise was additionally demonstrated on the basis of low statistic images of the hardware phantom.

In two patient studies we showed that the proposed motion correction strategy significantly improves the image quality of cardiac PET. First, 20 minute dual gated acquisitions with relatively high SNRs were corrected for 21 patients with known coronary artery disease. Second, the data was cropped to a clinically more realistic time of 3 minutes for each patient. VAMPIRE achieved accurate results that resemble cardiac and respiratory motion in both cases across all patients. The motion of body tissue can be adequately modeled by hyperelastic regularization, even in presence of severe heart defects, cf. Fig. 7. On the one hand, this is indicated by the appropriate Jacobian ranges that guarantee invertibility of the estimated transformations. On the other hand, visual inspection of Fig. 8 reveals that the estimated transformations for each individual gate are smooth and the transformations vary smoothly between the different gates. Hyperelastic regularization further leads to robustness of VAMPIRE against noise which was substantiated by a low average error of 0.73 mm between the motion estimates of the low statistic 3 minutes scans (each gate is formed over only 7.2 s) and the idealized 20 minutes scans. For the 20 minutes scan, the reduction of the COM to $0.723 \pm 0.212$ mm indicates a subvoxel accuracy. The maximum deformation values represents a typical value for respiratory motion [53]. After motion correction solely noise induced speckles remain in the difference images (Fig. 6(f), 11(f), and Fig. 9) and thus the subsequent averaging significantly improves the image quality (Fig. 6(g) and 11(g)). The average images combine the reduced amount of motion of the reference gate with the low noise of the image without gating. A low computation time is mandatory for clinical applicability. As all gates can be processed simultaneously, the relatively short registration time for a single gate can be interpreted as the total processing time for one patient.

The amplitude based gating scheme used in this paper was shown to perform better than time based methods [17]. On the one hand, each gate is reconstructed with the same statistic which allows us to use the same regularization parameters. On the other hand, gates can vary in the amount of respiratory motion as intervals of infrequent breathing phases are merged. The analysis of a compromise of statistic and amount of motion for our purposes is left for future work. The question of the optimal number of dual gates as in [40] should be carried out in connection with the choice of the respiratory gating scheme.

In this work, the focus was laid on obtaining accurate and realistic motion estimates that are used for subsequent averaging of the aligned images. We are positive that further improvements of image quality can be achieved by incorporating the transformation into a motion compensated reconstruction as proposed in [36]. Future work will also be devoted to entering the mass-preservation assumption into a joint reconstruction of image and motion [8, 10]. Attenuation correction of the data after motion correction is essential for further quantitative

analysis in clinical practice and will thus be considered in these approaches.

We will investigate a spatial-temporal extension in the spirit of [29] to further improve the robustness of motion estimation against low SNRs. A generalized mass-preserving transformation model can reasonably be applied to multi-modal data as well, e.g., registration of gated PET and an attenuation map. Hence, generalizations to multimodality similarity measures like mutual information (MI) [60] or normalized gradient fields (NGF) [24] are desirable.

The approximately incompressible myocardial tissue should be accompanied by a Jacobian determinant of roughly one [29]. Let us assume that the acquired data would not be affected by partial volume effect. Then, the assumption of mass-preservation is valid and our model can be used for motion estimation, which would result in Jacobian values of approximately one for myocardial tissue. In reality the data is, however, affected by partial volume effects. We can observe two consequent phenomena: 1) The PVE leads to intensity modulations of the constant myocardial uptake. 2) The total amount of myocardial activity remains unaffected. Hence, mass-preservation is a valid assumption and becomes – because intensities of corresponding points are not directly correlated any more – in a certain way mandatory [22]. Estimating the underlying motion out of PVE affected data is a challenging task and we have no doubt, that errors are introduced. Given the highly realistic ground truth motion of the XCAT software phantom (obtained with tagged MRI) an error of 1.624 mm on PVE disturbed XCAT images indicates that such possible errors are kept low.

As the scans are acquired one hour post injection, the $^{18}$F-FDG tracer will have accumulated almost entirely in the muscle tissue. Hence, we can assume static myocardial activity. This prevents possible artifacts due to varying average activities in different gates in regions like, e.g., the blood pool. However, due to different behavior of tissue (incompressibility of myocardial tissue), a non uniform regularization model might be interesting [29]. In this work, we decided not to choose such an approach to avoid the additional segmentation step which might be error-prone in our case of patients with coronary artery disease. However, in our future work we will investigate if a non uniform regularization model in combination with the presented Vampire approach might still improve our results. Related to this, the applicability of our method to perfusion tracers and dynamic scanning procedures might possibly not be given or needs at least further modification.

The mass-preserving registration algorithm Vampire will be made freely available as a plug-in for Fair [44].

In conclusion, we propose a novel image registration approach to motion correction in thoracic PET. The major improvement is the incorporation of a mass-preserving transformation model for motion estimation. We show that by entering this prior knowledge the presented Vampire algorithm robustly reduces both cardiac and respiratory motion to a very high extent in a clinical setting at feasible computational costs.

# 5 Acknowledgments

The authors would like to thank the anonymous reviewers for their valuable comments which have led to an considerable improvement of the manuscript. Further thanks go to Thomas Kösters for providing his reconstruction software EMrecon used for the reconstruction of the PET datasets. The list mode-driven gating was performed with the help of Florian Büther and his gating software. Especially, we thank Jan Modersitzki for his advise regarding the implementation and for making his Fair toolbox freely available. We would also like to thank Bernd Fischer, Christoph Brune and Mohammad Dawood for fruitful discussions and Björn Czekalla and Bertold Könemann for assistance with the phantom measurement.

# References

[1] A.M. Alessio and P.E. Kinahan. Application of a spatially variant system model for 3-D whole-body PET image reconstruction. *ISBI, IEEE*, pages 1315–1318, 2008.

[2] Vincent Arsigny, Olivier Commowick, Nicholas Ayache, and Xavier Pennec. A fast and log-euclidean polyaffine framework for locally linear registration. *J. Math. Imaging Vis.*, 33(2):222–238, 2009.

[3] Brian B. Avants, P. Thomas Schoenemann, and James C. Gee. Lagrangian frame diffeomorphic image registration: Morphometric comparison of human and chimpanzee cortex. *Med. Image Anal.*, 10(3):397–412, June 2006.

[4] W. Bai and M. Brady. Respiratory motion correction in PET images. *Phys. Med. Biol.*, 54:2719–2736, 2009.

[5] W. Bai and M. Brady. Spatio-temporal image registration for respiratory motion correction in PET. In *ISBI, IEEE*, pages 426–429, Piscataway, NJ, USA, 2009. IEEE Press.

[6] W. Bai and M. Brady. Motion correction and attenuation correction for respiratory gated PET images. *IEEE Trans. Med. Imag.*, 30(2):351–365, 2011.

[7] Thomas Beyer, Gerald Antoch, Todd Blodgett, Lutz F. Freudenberg, Tim Akhurst, and Stephan Mueller. Dual-modality PET/CT imaging: the effect of respiratory motion on combined image quality in clinical oncology. *Eur. J. Nucl. Med. Mol. I.*, 30:588–596, 2003.

[8] M. Blume, A. Martinez-Möller, A. Keil, N. Navab, and M. Rafecas. Joint reconstruction of image and motion in gated positron emission tomography. *IEEE Trans. Med. Imag.*, 29(11):1892–1906, November 2010.

[9] N. Boussion, C. Cheze Le Rest, M. Hatt, and D. Visvikis. Incorporation of wavelet-based denoising in iterative deconvolution for partial volume correction in whole-body PET imaging. *Eur. J. Nucl. Med. Mol. I.*, 36:1064–1075, 2009.

[10] C. Brune. *4D Imaging in Tomography and Optical Nanoscopy*. PhD thesis, University of Münster, 2010.

[11] F. Büther, M. Dawood, L. Stegger, F. Wübbeling, M. Schäfers, O. Schober, and K.P. Schäfers. List mode-driven cardiac and respiratory gating in PET. *J. Nucl. Med.*, 50(5):674–681, 2009.

[12] H. Chang and J.M. Fitzpatrick. A technique for accurate magnetic resonance imaging in the presence of field inhomogeneities. *IEEE Trans. Med. Imag.*, 11(3):319–329, 1992.

[13] S.R. Cherry and M. Dahlbom. *PET - Molecular Imaging and Its Biological Applications*, chapter PET: Physics, Instrumentation, and Scanners, pages 1–125. Springer, 2004.

[14] P.G. Ciarlet. *Mathematical elasticity: Three-dimensional elasticity*. North Holland, 1988.

[15] M. Dawood, F. Büther, X. Jiang, and K.P. Schäfers. Respiratory motion correction in 3-D PET data with advanced optical flow algorithms. *IEEE Trans. Med. Imag.*, 27(8):1164–1175, 2008.

[16] M. Dawood, N. Lang, Xiaoyi Jiang, and K. P. Schafers. Lung motion correction on respiratory gated 3-D PET/CT images. *IEEE Trans. Med. Imag.*, 25(4):476–485, 2006.

[17] Mohammad Dawood, Florian Büther, Norbert Lang, Otmar Schober, and Klaus P Schäfers. Respiratory gating in positron emission tomography: A quantitative comparison of different gating schemes. *Med. Phys.*, 34(7):3067–3076, 2007.

[18] M. Droske and M. Rumpf. A variational approach to nonrigid morphological image registration. *SIAM J. Appl. Math.*, 64(2):668–687, 2003.

[19] Y.E. Erdi, S.A. Nehmeh, T. Mulnix, J.L. Humm, and C.C. Watson. PET performance measurements for an LSO-based combined PET/CT scanner using the national electrical manufacturers association NU 2-2001 standard. *J. Nucl. Med.*, 45(5):813–21, 2004.

[20] L. Fin, P. Bailly, J. Daouk, and M.-E. Meyer. Motion correction based on an appropriate system matrix for statistical reconstruction of respiratory-correlated PET acquisitions. *Comput. Meth. Prog. Bio.*, 96(3):e1–e9, 2009.

[21] B. Fischer and J. Modersitzki. Ill-posed medicine—an introduction to image registration. *Inverse Probl.*, 24:034008, 2008.

[22] F. Gigengack, L. Ruthotto, M. Burger, C.H. Wolters, X. Jiang, and K.P. Schaefers. Motion correction of cardiac PET using mass-preserving registration. In *NSS/MIC Conference Record, IEEE*, 2010.

[23] G.W. Goerres, C. Burger, E. Kamel, B. Seifert, A.H. Kaim, A. Buck, T.C. Buehler, and G.K. von Schulthess. Respiration-induced attenuation artifact at PET/CT: Technical considerations. *Radiology*, 226(3):906–910, 2003.

[24] Eldad Haber and Jan Modersitzki. Intensity gradient based registration and fusion of multi-modal images. *Methods of Information in Medicine*, 46(3):292–299, 2007.

[25] H.M. Hudson and R.S. Larkin. Accelerated image reconstruction using ordered subsets of projection data. *IEEE Trans. Med. Imag.*, 13(4):601–609, 1994.

[26] M.W. Jacobson and J.A. Fessler. Joint estimation of image and deformation parameters in motion-corrected PET. In *IEEE Nuc. Sci. Symp. Med. Im. Conf.*, volume 5, pages 3290–3294, 2003.

[27] G.J. Klein. Forward deformation of PET volumes using material constraints. In *WBIA, IEEE*, pages 64–71, 1998.

[28] G.J. Klein. Forward deformation of PET volumes using non-uniform elastic material constraints. In *IPMI*, pages 358–363, 1999.

[29] G.J. Klein and R.H. Huesman. Four dimensional processing of deformable cardiac PET data. *Med. Image Anal.*, 6(1):29–46, 2002.

[30] G.J. Klein, B.W. Reutter, M.H. Ho, J.H. Reed, and R.H. Huesman. Real-time system for respiratory-cardiac gating in positron tomography. *IEEE T. Nucl. Sci.*, 45(4):2139–2143, 1998.

[31] G.J. Klein, B.W. Reutter, and R.H. Huesman. Non-rigid summing of gated PET via optical flow. In *NSS Conference Record, IEEE*, volume 2, 1996.

[32] T. Kokki, H. Sipilä, M. Teräs, T. Noponen, N. Durand-Schaefer, R. Klén, and J. Knuuti. Dual gated PET/CT imaging of small targets of the heart: Method description and testing with a dynamic heart phantom. *J. Nucl. Cardiol.*, 17:71–84, 2009.

[33] T. Kösters, K.P. Schäfers, and F. Wübbeling. EMrecon: An expectation maximization based image reconstruction framework for emission tomography data. In *NSS/MIC Conference Record, IEEE*, 2011.

[34] T. Kösters. *Derivation and analysis of scatter correction algorithms for quantitative positron emission tomography.* PhD thesis, University of Münster, 2010.

[35] F. Lamare, T. Cresson, J. Savean, C. Cheze Le Rest, A.J. Reader, and D. Visvikis. Respiratory motion correction for PET oncology applications using affine transformation of list mode data. *Phys. Med. Biol.*, 52(1):121–140, 2007.

[36] F. Lamare, MJ Ledesma Carbayo, T. Cresson, G. Kontaxakis, A. Santos, C.C. Le Rest, AJ Reader, and D. Visvikis. List-mode-based reconstruction for respiratory motion correction in PET using non-rigid body transformations. *Phys. Med. Biol.*, 52(17):5187–5204, 2007.

[37] F. Lamare, M. Teras, T. Kokki, H. Fayad, O. Rimoldi, P.G. Camici, J. Knuuti, and D. Visvikis. Correction of respiratory motion in dual gated cardiac imaging in PET/CT. In *NSS/MIC Conference Record, IEEE*, pages 5264–5269, 2008.

[38] G. Lucignani. Respiratory and cardiac motion correction with 4D PET imaging: Shooting at moving targets. *Eur. J. Nucl. Med. Mol. I.*, 36(2):315–319, 2009.

[39] F. Büther X. Jiang M. Burger O. Schober M. Schäfers K.P. Schäfers M. Dawood, C. Brune. A continuity equation based optical flow method for cardiac motion correction in 3D PET data. In *MICCAI, LNCS*, volume 6326, pages 88–97, 2010.

[40] L. Stegger X. Jiang O. Schober M. Schäfers K.P. Schäfers M. Dawood, F. Büther. Optimal number of respiratory gates in positron emission tomography: A cardiac patient study. *Med. Phys.*, 36(5):1775–1784, 2009.

[41] Bernard Anthony Mair, David R. Gilland, and Jing Sun. Estimation of images and nonrigid deformations in gated emission CT. *IEEE Trans. Med. Imag.*, 25(9):1130–1144, 2006.

[42] Thibault Marin and Jovan G. Brankov. Deformable left-ventricle mesh model for motion-compensated filtering in cardiac gated SPECT. *Med. Phys.*, 37(10):5471–5481, 2010.

[43] Axel Martinez-Möller, Darko Zikic, René Botnar, Ralph Bundschuh, William Howe, Sibylle Ziegler, Nassir Navab, Markus Schwaiger, and Stephan Nekolla. Dual cardiac–respiratory gated PET: Implementation and results from a feasibility study. *Eur. J. Nucl. Med. Mol. I.*, 34:1447–1454, 2007.

[44] J. Modersitzki. *FAIR: Flexible Algorithms for Image Registration*. SIAM, Philadelphia, 2009.

[45] R Narayanan, J A Fessler, H Park, and C R Meyer. Diffeomorphic nonlinear transformations: A local parametric approach for image registration. In *IPMI*, pages 174–185, 2005.

[46] J. Olesch, L. Ruthotto, H. Kugel, Stefan Skare, B. Fischer, and C. H. Wolters. A variational approach for the correction of field-inhomogeneities in EPI sequences. In *SPIE Medical Imaging Conference, San Diego, USA*, 2010.

[47] Medhat M. Osman, Christian Cohade, Yuji Nakamoto, and Richard L. Wahl. Respiratory motion artifacts on PET emission images obtained using CT attenuation correction on PET-CT. *Eur. J. Nucl. Med. Mol. I.*, 30:603–606, 2003.

[48] M.M. Osman, C. Cohade, Y. Nakamoto, L.T. Marshall, J.P. Leal, and R.L. Wahl. Clinically significant inaccurate localization of lesions with PET/CT: Frequency in 300 patients. *J. Nucl. Med.*, 44(2):240–243, 2003.

[49] D. Rueckert, P. Aljabar, R. A. Heckemann, J. V. Hajnal, and A. Hammers. Diffeomorphic Registration Using B-Splines. In R. Larsen, M. Nielsen, and J. Sporring, editors, *MICCAI*, volume 4191 of *LNCS*, pages 702–709. Springer, 2006.

[50] L. Ruthotto. Mass-preserving registration of medical images. German diploma thesis (mathematics), Institute for Computational and Applied Mathematics, University of Münster, march 2010.

[51] K.P. Schäfers, B. Könemann, B. Czekalla, K. Bolwin, F. Büther, M. Fieseler, H. Braun, S. Ziegler, and H.H. Quick. Human thorax phantom for simulation of respiratory and cardiac motion in PET/MRI: Development and first measurements. In *NSS/MIC Conference Record, IEEE*, 2011.

[52] Hanno Schumacher, Jan Modersitzki, and Bernd Fischer. Combined reconstruction and motion correction in SPECT imaging. *IEEE T. Nucl. Sci.*, 56:73–80, 2009.

[53] A.J. Schwarz and M.O. Leach. Implications of respiratory motion for the quantification of 2D MR spectroscopic imaging data in the abdomen. *Phys. Med. Biol.*, 45(8):2105–2116, 2000.

[54] W.P. Segars. *Development and application of the new dynamic NURBS-based cardiac-torso (NCAT) phantom.* Biomedical engineering, University of North Carolina, Chapel Hill, NC, 2001.

[55] W.P. Segars, M. Mahesh, T.J. Beck, E.C. Frey, and B.M.W. Tsui. Realistic CT simulation using the 4d XCAT phantom. *Med. Phys.*, 35(8):3800–3808, 2008.

[56] L. A. Shepp and Y. Vardi. Maximum likelihood reconstruction for emission tomography. *IEEE Trans. Med. Imag.*, 1(2):113–122, 1982.

[57] Mika Teräs, Tommi Kokki, Nicolas Durand-Schaefer, Tommi Noponen, Mikko Pietilä, Jan Kiss, Erika Hoppela, Hannu Sipilä, and Juhani Knuuti. Dual-gated cardiac PET–clinical feasibility study. *Eur. J. Nucl. Med. Mol. I.*, 37:505–516, 2010.

[58] K. Thielemans, E. Asma, and R.M. Manjeshwar. Mass-preserving image registration using free-form deformation fields. In *NSS/MIC Conference Record, IEEE*, 2009.

[59] H. Ue, H. Haneishi, H. Iwanaga, and K. Suga. Nonlinear motion correction of respiratory-gated lung SPECT images. *IEEE Trans. Med. Imag.*, 25(4):486–495, 2006.

[60] Paul A. Viola. *Alignment by maximization of mutual information.* PhD thesis, Massachusetts Institute of Technology, 1995.

[61] Y. Wang, E. Vidan, and G.W. Bergman. Cardiac motion of coronary arteries: Variability in the rest period and implications for coronary MR angiography. *Radiology*, 213(3):751–758, 1999.

[62] Y. Yin, E.A. Hoffman, and C.L. Lin. Mass preserving nonrigid registration of CT lung images using cubic B-spline. *Med. Phys.*, 36(9):4213–4222, 2009.